RESEARCH ARTICLE | FEBRUARY 04 2025

Dynamic drop penetration of vertically oriented fiber arrays

Gene Patrick S. Rible ; Visalsaya Chakpuang; Aidan D. Holihan; Hannah P. Sebek; Hannah H. Osman; Kyle R. Brown; Wei Wang ; Andrew K. Dickerson

Physics of Fluids 37, 022108 (2025)
https://doi.org/10.1063/5.0246986

Physics of Fluids ARTICLE pubs.aip.org/aip/pof

Dynamic drop penetration of vertically oriented fiber arrays

Cite as: Phys. Fluids **37**, 022108 (2025); doi: 10.1063/5.0246986
Submitted: 5 November 2024 · Accepted: 3 January 2025 ·
Published Online: 4 February 2025

Gene Patrick S. Rible, Visalsaya Chakpuang, Aidan D. Holihan, Hannah P. Sebek, Hannah H. Osman, Kyle R. Brown, Wei Wang, and Andrew K. Dickerson[a)]

AFFILIATIONS

Department of Mechanical, Aerospace, and Biomedical Engineering, University of Tennessee, Knoxville, Tennessee 37996, USA

[a)]Author to whom correspondence should be addressed: ad@utk.edu

ABSTRACT

This experimental work investigates the impact dynamics of drops on vertically oriented, three-dimensional-printed (3D-printed) fiber arrays with variations in packing density, fiber arrangement, and wettability. These fiber arrays are inspired by mammalian fur, and while not wholly representative of the entire morphological range of fur, they do reside within its spectrum. We define an aspect ratio, a modified fiber porosity relative to the drop size, that characterizes various impact regimes. Using energy conservation, we derive a model relating drop penetration depth in vertical fibers to the Weber number. In sparse fibers where the Ohnesorge number is less than 4×10^{-3}, penetration depth scales linearly with the impact Weber number. In hydrophobic fibers, density reduces penetration depth when the contact angle is sufficiently high. Hydrophilic arrays have greater penetration than their hydrophobic counterparts due to capillarity, a result that contrasts the drop impact-initiated infiltration of horizontal fibers. Vertical capillary infiltration of the penetrated liquid is observed whenever the Bond number is less than 0.11. For hydrophilic fibers, we predict that higher density will promote drop penetration when the contact angle is sufficiently low. Complete infiltration by the drop is achieved at sufficient times regardless of drop impact velocity.

I. INTRODUCTION

Fur is a prominent feature of mammals that serves a myriad of functions by way of its intricate structure. Fur provides mammalian skin with physical protection from injury and infection[1] and facilitates a mammal's ability to maintain homeostasis by providing thermal insulation,[2–4] reflecting ultraviolet radiation,[5] and repelling water.[6,7] Animals like sea otters grow dense fur coats[4] to keep the water far away from their skin, while pigs grow sparse and short hair[8] to facilitate convection. The complex interaction of variables of mammalian fur that keep the skin dry is understudied. Understanding drop impact dynamics onto mammalian fur can improve our understanding of water resistance.

Across mammals, there exists a vast diversity in fur characteristics including variations in texture, length, orientation, density, and location.[9] From the woolen, hollow hair of the newborn reindeer developed to insulate against the extreme cold,[10] to the sparse fur of the Asian elephant adapted for thermoregulation in hot climates,[11] and the dense, interwoven fur of the sea otter designed to trap air bubbles between each individual fiber,[4,7,12] mammalian fur evolved in response to environmental pressures. Despite the various morphological differences, mammalian fur is functionally a porous medium consisting of dense or sparsely packed fibers arranged in an array. Mammalian fur can exhibit a wide range of directional orientations ranging from flat to vertical,[13] influencing its interaction with environmental perturbations, such as rainfall. We note that despite popular belief, mammalian fibers are not circular.[14,15] For a drop impacting a single horizontal fiber, the wedge-like shape has been shown to promote drop fragmentation.[16]

There have been numerous studies of drop impacts onto various surfaces, from single fibers with infinite intrinsic porosity, to porous materials with intermediate intrinsic porosity, and solid surfaces with zero intrinsic porosity. Intrinsic porosity is the fraction of void within the material to the total volume, which, in the case of fiber arrays, may be recast as an "aspect ratio".[17] $\boldsymbol{AR}$, the ratio of the area projection of the spaces in between fibers a to the total area occupied the fibers of width ℓ,

$$\boldsymbol{AR} = \frac{a}{\ell + a}. \tag{1}$$

Solid surfaces have $\boldsymbol{AR} = 0$; singular fibers $\boldsymbol{AR} = 1$; and porous media $0 < \boldsymbol{AR} < 1$. Greater values of $\boldsymbol{AR}$ will intuitively result in easier penetration by an impacting drop. However, Eq. (1) is ignorant of drop size, thus insufficient to describe changes in impact behavior.[17–22] The inclusion of drop size is captured in a modified aspect ratio, $\boldsymbol{AR}$, multiplied by the ratio of fiber-plus-gap unit $\ell + a$ to the drop size, D_0, as done in previous papers:[17,23,24]

$$\boldsymbol{AR}^* = \boldsymbol{AR}\frac{\ell + a}{D_0} = \frac{a}{D_0}, \quad \text{for} \quad \ell + a < D_0. \tag{2}$$

The ability of a drop to penetrate an array is now cursorily described by $\boldsymbol{AR}^*$ as used in our previous work on drops impacting horizontal fibers.[17]

On porous surfaces, the surface roughness and impact Weber number $We = \rho U^2 D_0/\sigma$, where ρ is the mass density and σ is the surface tension of water, govern the splash threshold.[25] The Reynolds number that uses a characteristic length based on surface roughness multiplied by the substrate porosity enhances drop deposition without splash.[23,25,26] For horizontal fiber arrays, hydrophilic fibers promote lateral drop spreading, preventing dynamic drop penetration into the array,[17] whereas hydrophobic arrays enhance penetration by promoting drop fragmentation along the penetration direction.[17,23] Denser fibers and staggered configurations reduce penetration compared with their sparser and aligned counterparts.

While studies done on vertically oriented fiber arrays are limited, existing research has characterized the behavior of drops on vertically oriented fibers, such as water collection on the fibers due to the capillarity.[27–30] In a vertical fiber array absent of gravitational forces, the contact line dissipation (or contact line friction) is largely responsible for arresting the drop, and penetration depth is largely influenced by fiber flexibility.[27] For micro-scale arrays, the drop can either remain on the surface or penetrate the fibers during impact. On hairy surfaces with millimetric "mesoscale" texture similar to our fiber arrays but with relatively short fibers, dissipating the kinetic energy of the drop has been rationalized through a balance of inertia, viscosity, and surface tension.[31] When the energy lost by passing through the hair fibers is equal to the initial kinetic energy of the drop, the drop reaches the base and is arrested. If the kinetic energy is greater, the drop spreads and can splash if the ratio of energy loss to kinetic energy is ≤ 0.2. For lower values of kinetic energy and greater viscosity, the drop will not reach the base or may not penetrate. In this work, we likewise use an energy balance, but instead of employing energy ratios to classify drop behavior, we predict the depth of penetration within the fiber array. Classifying the drop according to the extent of rebound, the presence of lateral trans-fiber motions, and capillary action, we provide an alternative regime map that complements the classifications made in the previous work.[31] Furthermore, we look at the effect of fiber wettability on the drop penetration dynamics of vertical fiber arrays as inspired by a result from a previous work[17] that hydrophilic horizontal fiber arrays resist dynamic drop penetration more than their hydrophobic counterparts. Here, we explore whether the same is true for vertical fiber arrays.

Previous studies on rough porous substrates deal with $\boldsymbol{AR}^* = 0 - 0.19$,[23,25,32–35] whereas previous fiber studies consider $\boldsymbol{AR}^* = 0.6 - 1$.[27,36–38] Although both the high and low modified aspect ratios have been studied, the gap $0.2 - 0.6$ remains understudied. Animal fur falls within the unstudied gap. For example, the gray wolf[39] has a fur density of $D \sim 100$ strands/cm^2 and a shaft diameter of ~ 0.01 cm,[39,40] which translates to an inter-fiber spacing of 0.09 cm. Assuming a drop diameter of 3 mm, the modified aspect ratio is 0.3, which falls in the unstudied range of 0.2 to 0.6 wherein the observed behavior differs from either extreme. Furthermore, our choice of drop size places the drop within the natural range of raindrop size,[41] but toward the larger end so that drops have sufficient momentum to penetrate our arrays. Exceedingly large drops are unstable as rainfall, and smaller drops may be unable to penetrate our arrays due to low momentum and too small to fragment. In this range, the impacting drop can slightly rebound upon hitting the fibers, but the array does not provide enough resistance to halt the momentum of the impacting drop. The penetrating liquid is subject to capillary forces from multiple fiber strands. This study investigates drop impact and penetration of vertically oriented fiber arrays with modified aspect ratios $0.2 - 0.6$ pictured in Fig. 1(a), filling in a part of the existing gap in the literature.

II. EXPERIMENTAL SECTION

A. Fur printing, morphology, and wettability

Our vertical fiber arrays are ablated versions of fiber arrays used in our previous study on horizontally oriented fibers.[17] Translucent fiber arrays are fabricated with photopolymer resin in a FlashForge Hunter digital light processing (DLP) resin 3D printer with a layer resolution of 25 μm and a pixel size of 62.5 μm. According to FlashForge, the cured resin has a tensile modulus of 48 MPa and a flexural modulus of 2250 MPa. A block of resin anchors fibers at each end to ensure fiber alignment during production and experimentation, as pictured in Fig. 1(a). The fiber/block structure is printed such that fibers are parallel to the build plate. Printer resolution and curing dynamics limit the length and density of the fibers, and we can manufacture without the fibers clumping into a unified mass during printing. After printing, the three-dimensional-printed (3D-printed) fibers are cut on one end with a laser cutter to be cantilevered.

A cross-sectioned experimental fiber is pictured in Fig. 1(a). Fibers are designed to be square in cross section with a dimension ℓ for the sake of printing, as illustrated in Fig. 1(b), but gravity causes the resin to flow into a wedge-like cross section during printing in the resin bath, as shown in Fig. 1(a). Therefore, the fibers have a cross-sectional width of 344 ± 26 μm (number of trials N = 18) and cross-sectional length 394 ± 50 μm (N = 18). The unintended wedge-like shape of mammalian fur fibers allows us to test the influence of cross section orientation on drop impact outcomes on horizontally oriented fiber arrays.[17]

Arrays are printed with three different permutations of inter-fiber spacing a to generate packing densities of approximately 50, 100, and 150 cm^{-2}, with an average error on a of 3.8%. We are, thus, able to investigate the effect of fiber density D on the penetration behavior, not previously explored.[31] We produce and test two packing configurations for each packing density, one in which all fibers are aligned in a square grid (aligned) and another in which fibers in an adjacent row are shifted laterally by $a/2$ (staggered), as shown in Fig. 1(b). Although the fiber alignment affects the drop impact dynamics when the fiber array is horizontally oriented,[17] the radial symmetry of the impacting drop allows staggered and aligned vertical fibers to be functionally equivalent. To the impacting drop, staggered arrays are simply aligned arrays rotated 45°, as shown in Fig. 1(b).

We make arrays hydrophobic through vapor deposition, grafting a heptadecafluoro-1, 1, 2, 2− tetrahydrodecyltrichlorosilane (FDTS) onto the surface[42,43] resulting in receding, equilibrium, and advancing

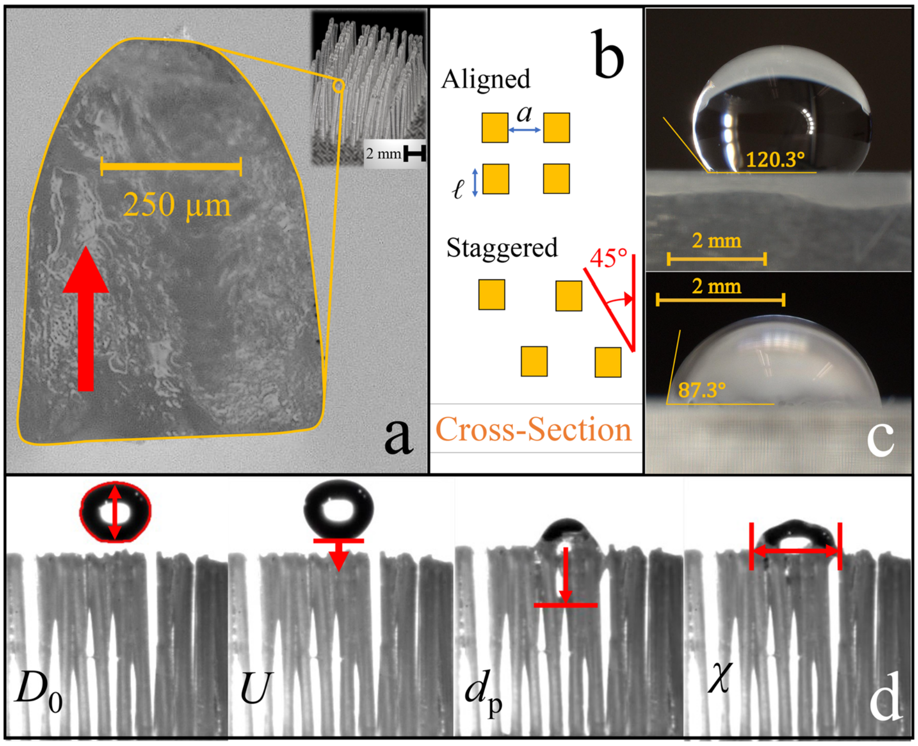

FIG. 1. 3D-printed vertical fiber arrays. (a) Freshly printed fiber arrays are ablated to be cantilevered and undergo surface treatment to change wettability. The red arrow denotes the printing direction. (b) Fiber strands of a sample are arranged in an aligned or staggered configuration. (c) Contact angles of water drops on hydrophobic (top) and hydrophilic (bottom) samples. (d) Dimensional impact parameters: drop diameter D_0, impact velocity U, penetration depth d_p, and lateral spread χ.

contact angles of $\theta_\mathrm{r} = 62.9 \pm 8.9°$ (number of trials N = 3), $\theta_\mathrm{e} = 120.3 \pm 8.1°$ (N = 3), and $\theta_\mathrm{a} = 128.8 \pm 7.6°$ (N = 3), respectively. The FDTS monolayer contributes less than 3 nm of thickness to the fibers.[44,45] The hydrophilic samples are modified using oxygen plasma to create hydroxyl groups on the fiber surface, resulting in no thickness change and contact angles $\theta_\mathrm{r} = 68.1 \pm 4.7°$ (N = 3), $\theta_\mathrm{e} = 87.3 \pm 1.2°$ (N = 3), and $\theta_\mathrm{a} = 112.2 \pm 6.4°$ (N = 3). The cured mounting blocks at the fiber array base as shown in Fig. 1(a) provide a flat surface on which we measure the contact angles of drops; the resulting sessile drops are pictured on both hydrophobic and hydrophilic samples in Fig. 1(c). Because the hydroxyl groups are highly reactive, all experiments with hydrophilic fibers in this work were completed within two days after sample preparation. The fibers are approximately 8 mm long after ablation and create a 10 mm × 10 mm array as seen by the impacting drop. The array size ensures that drops do not cross the array boundary over the course of impact. Because our fibers are longer than a previous work,[31] we are able to study penetration depth behavior depending on drop properties, fiber properties, and initial impact conditions. The width of our fiber cross section is $\ell \approx 350\ \mu$m, as shown in Fig. 1(b).

B. Experimental methodology and principle measurements

For simplicity, drops of a fixed diameter $D_0 = 2.64 \pm 0.17$ mm (N = 111) are released from a needle positioned at heights $h = 3, 12,$ and 24 mm above a fiber array with impact Reynolds number $Re = \rho U D_0/\mu = 376 - 1980$, where μ is the dynamic viscosity of water. A modified Reynolds number $Re^* = \rho U a/\mu = 99 - 1025$ based on the inter-fiber spacing[17,46] better characterizes the flow in our fiber arrays. The Ohnesorge number is $Oh = \mu/\sqrt{\rho\sigma a} = 2.9 \times 10^{-3} - 5.3 \times 10^{-3}$. Impacts are filmed with two, synchronized Photron Nova S6 cameras at 3000 fps, with a resolution of approximately 25 pixels/mm. An oblique view camera is used to verify impact location from above the fiber but does not provide quantitative data. Between trials, samples are dried with compressed lab air and never contacted human skin. Videos captured by a front view camera normal to the fiber array sample are binarized in MATLAB with no imposed dilation or erosion. From binarized video frames, we measure drop diameter D_0, drop velocity U, penetration depth d_p, and the drop width χ ($\chi = D_0$ pre-impact) labeled in Fig. 1(d).

C. Dimensionless parameters

The principle quantities measured during and following impact are normalized by spherical drop diameter D_0 to form

$$\breve{d}_\mathrm{p} = d_\mathrm{p}/D_0, \quad \text{and} \quad \breve{\chi} = \chi/D_0. \tag{3}$$

We nondimensionalize time t by the timescale of impact such that the dimensionless inertial time $\tau = tU/D_0$. The moment of drop contact corresponds to $\tau = 0$. We also denote three distinct moments during the infiltration of the fibers. The first is when the drop reaches its widest lateral extent to achieve χ_m and $\breve{\chi}_\mathrm{m} = \chi_\mathrm{m}/D_0$, a wetting position it may or may not hold steadily. The second is when the drop penetrates deepest into the array to achieve $d_\mathrm{p,m}$ and $\breve{d}_\mathrm{p,m} = d_\mathrm{p,m}/D_0$. In vertical fibers, $\breve{d}_\mathrm{p,m}$ is equal to the steady-state penetration depth, which is not always true in horizontal fiber arrays.[17] The third is when the drop achieves its final resting position where neither wetted width nor depth measurably changes in the timescale of our videos. We denote steady-state values of time-dependent quantities such as lateral deformation by an "s" subscript: $\breve{\chi}_s$.

III. RESULTS AND DISCUSSION

A. Anisotropic fiber misalignment induces lateral drop motion

In a previous study on a drop impacting horizontally oriented fiber arrays, we identified eight impact classifications based on the occurrence of vertical "jet-like rebound," fragmentation, bouncing, and capillary spreading of the impacting drop.[17] In the range of *We* values we investigate, we observe no drop fragmentation, bouncing, or lateral capillary spreading in vertical fibers. The anisotropic misalignment of the fibers coupled with the stochastic location of impact on the fiber arrays results in lateral trans-fiber drop motion, which we classify into two categories. A "wave" is a lateral oscillation as shown in Fig. 2(b), and a "bisection" is the splitting of the drop into two components that have seemingly disconnected motion as depicted in Fig. 2(b) and may or may not be a unified mass. Wave and bisection can occur simultaneously as shown in Fig. 2(c). The anisotropy that occurs haphazardly in areas of our fiber arrays is not quantified, although it is promoted by fiber density. As with horizontally oriented fibers,[17] fiber spacing $\boldsymbol{AR}^*$, configuration, cross-sectional profile, contact angle, and drop impact velocity U collectively govern the expression of such impact classifications.

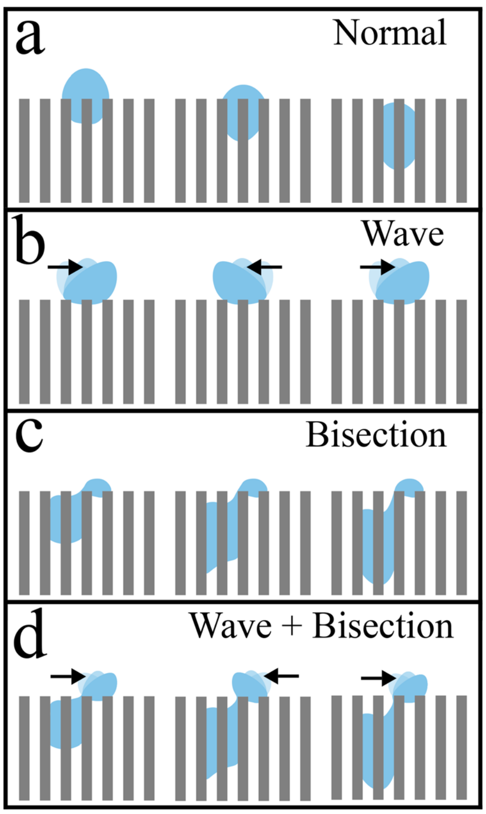

FIG. 2. Illustration of trans-fiber motions: (a) Normal, (b) Wave, (c) Bisection, and (d) Wave+Bisection. Image sequences from left to right.

Eight impact classifications for drops impacting vertically oriented fibers are shown in Fig. 3 (multimedia available online). The advancing contact angles in Fig. 3 for dense arrays appear hydrophilic due to shadowing, but upon closer inspection, the advancing angles are indeed $> 90°$ as shown in Fig. 4 (multimedia available online). In horizontally oriented fibers, axial capillary action promotes the lateral spreading of drops within the fibers, thereby reducing penetration.[17] A plot of normalized maximum penetration depth vs dimensionless time is shown in Fig. 5(d) for a drop that impacts the base of the array. We predict that in the hypothetical penetration depth, the drop would achieve with long fibers by assuming the drops decelerate at a constant rate (Sec. III B). When the fibers are vertically oriented to the penetrating drop, axial capillary action is vertical and promotes penetration while preventing spreading. Consequently, we observe drops reaching the bottom of the fiber array samples where the fiber strands attach to the base, as shown in Fig. 5(d) (multimedia available online). When the drop reaches the base of the samples, the drop can spread laterally either through momentum dissipation or capillary action at the base of the fiber array. We plot $\boldsymbol{AR}^*$ vs *We* for aligned (A) and staggered (S) fibers in Figs. 5(a) and 5(b). We classify impacts according to the presence or absence of trans-fiber drop motions, the presence or absence of capillary action, and the sharpness of rebound. The various impact classifications cluster in parameter space. Lateral wave-like motion (blue and magenta symbols) is more likely to occur in lower *We* values and is promoted by hydrophobicity. Bisection (red and magenta symbols) and capillary action (◃, ▹, ►) are more likely to occur at lower $\boldsymbol{AR}^*$ and are promoted by hydrophilicity. A solid right triangle (►) indicates capillary penetration, whereas a hollow left or right triangle (◃ or ▹) indicates spreading at the array base due to capillary action, momentum dissipation, or a combination of both mechanisms. The product of *We* and $\boldsymbol{AR}^*$ is a useful indicator of drop impact behavior as observed in previous studies on drops impacting porous media and textile fibers.[23,24] In textile fibers, for example, the critical mesh size to prevent penetration is inversely proportional[23] to the *We*, where the textile mesh size is analogous to $\boldsymbol{AR}^*$ in this work. Although some impacts exhibit a pronounced drop rebound above the surface ("rebound" ▲), some impacts show a subtle rebound ("little rebound" ● and ○), whereas other impacts exhibit no rebound at all ("no rebound" ▽ and ▼). In vertical fibers, rebound is promoted by low $\boldsymbol{AR}^*We$ as shown in Figs. 5(c)—a similar behavior is observed of drops impacting horizontally oriented fibers.[17] The likelihood of rebound is independent of fiber wettability in the range of fiber densities we tested. Verifying whether fragmentation can occur at higher *We* for a certain range of $\boldsymbol{AR}^*$ and if certain liquid or fiber properties promote drop fragmentation in vertical fiber arrays is an area for future work.

A high $\boldsymbol{AR}^*We$ is enabled by sparser arrays and faster impact speeds resulting in reduced resistance to inertial liquid penetration so that only the inertial part of the impact is observed before the drop hits the bottom of the fiber array. Solid symbols (■) represent impacts where the drop did not reach the bottom of the fiber array, whereas hollow symbols (□) represent impacts where the drop penetrated to the bottom of the fiber array. Because of the length limitations of our fiber array samples, vertical capillary action is not observed for higher $\boldsymbol{AR}^*We$ in our experiments, but we posit that it will be present at a latter τ for longer fibers. When considering only impacts that did not hit the bottom of our fiber arrays, vertical capillary action can occur whenever the Bond number $Bo = \rho g a^2/\sigma \leq 0.11$, represented by the little

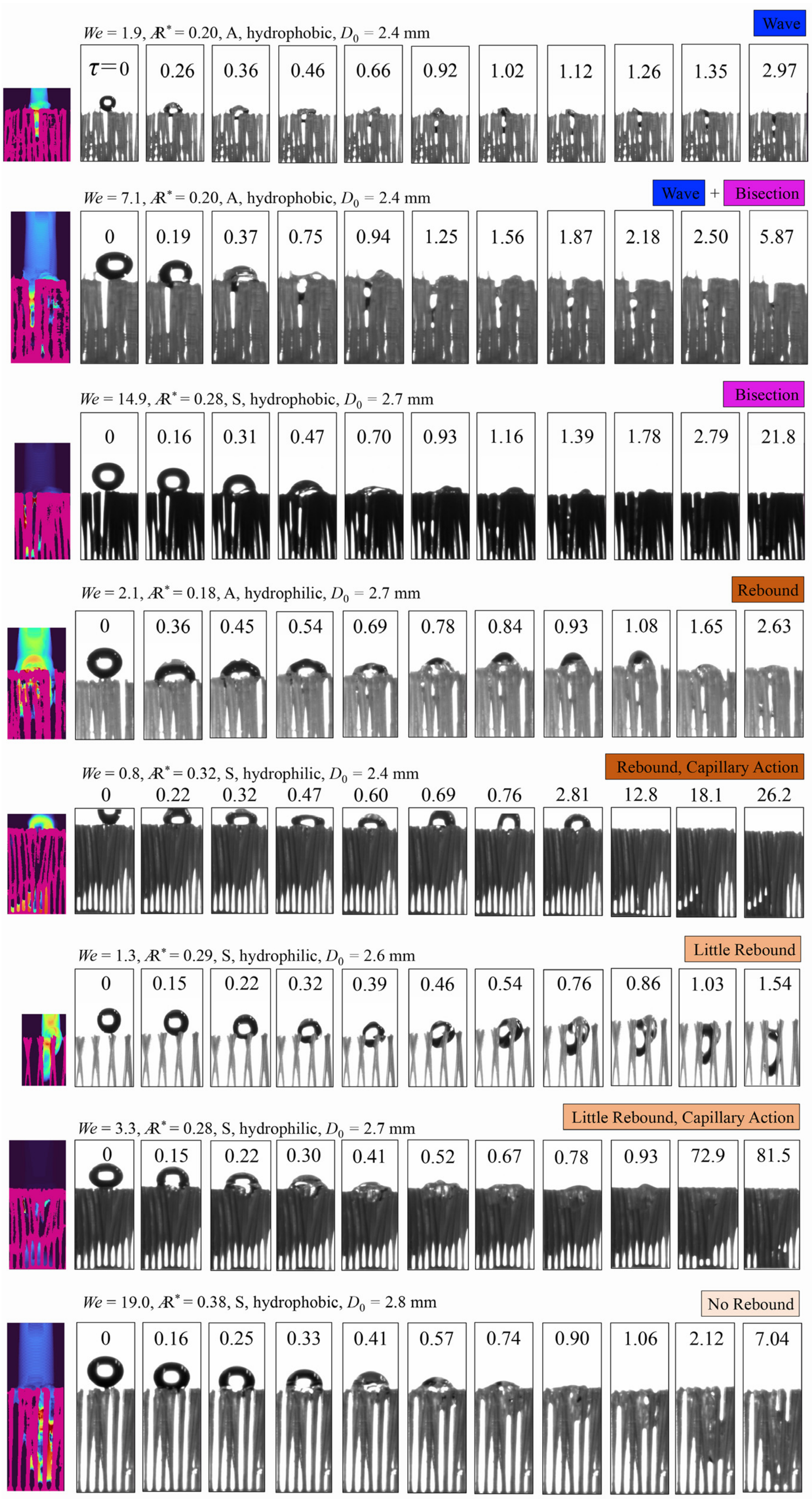

FIG. 3. Image sequences of observed impact classifications. The leftmost column shows normalized, temporal heat maps that quantify drop residence time and provide a characteristic image for each impact. Impact classification names are highlighted with a color based on vertical rebound motion or lateral trans-fiber motions wave and rebound. Dimensionless time stamps in each frame (τ) are chosen to show the entirety of the impact and are not linearly spaced in time. Multimedia available online.

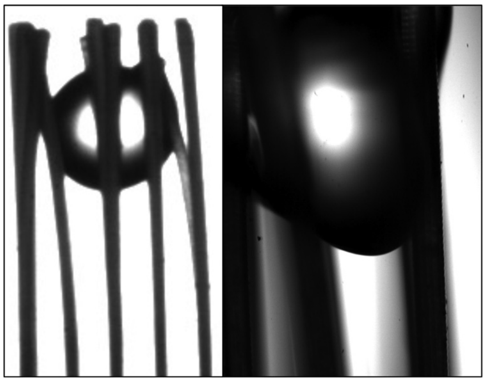

FIG. 4. The advancing contact angles appear hydrophilic in our fiber arrays (left) due to shadow, but a closer inspection shows they are $> 90°$ (right). Multimedia available online.

rebound, capillary action (LRC) impacts (►) in Figs. 5(a) and 5(b). Impact classifications that do not exhibit vertical capillary action reach steady-state in a relatively shorter dimensionless time. For example, the drop on the seventh row of Fig. 3 has an impact sequence that is more than $50 \times$ longer than the impact on the sixth row. A profile of all impact classifications, capturing the transient rebound, capillary action, and lateral trans-fiber motions that arise during impact is captured in the normalized heat maps in the leftmost column of Fig. 3. The reddest colors indicate a higher incidence of drop spatial residence, whereas the bluest colors indicate the most transience. In our vertically oriented fiber arrays where the strands lean and obscure one another, especially at higher D, the heat maps allow us to distinguish water from fiber.

The entire drop resides within the fibers at steady state. Moreover, $\breve{\chi}_m$ typically occurs close to the tip of the fibers in the first few moments after the drop first touches the tip of the fibers ($\tau < 1$), as shown in Fig. 6(a) (multimedia available online). Although we do

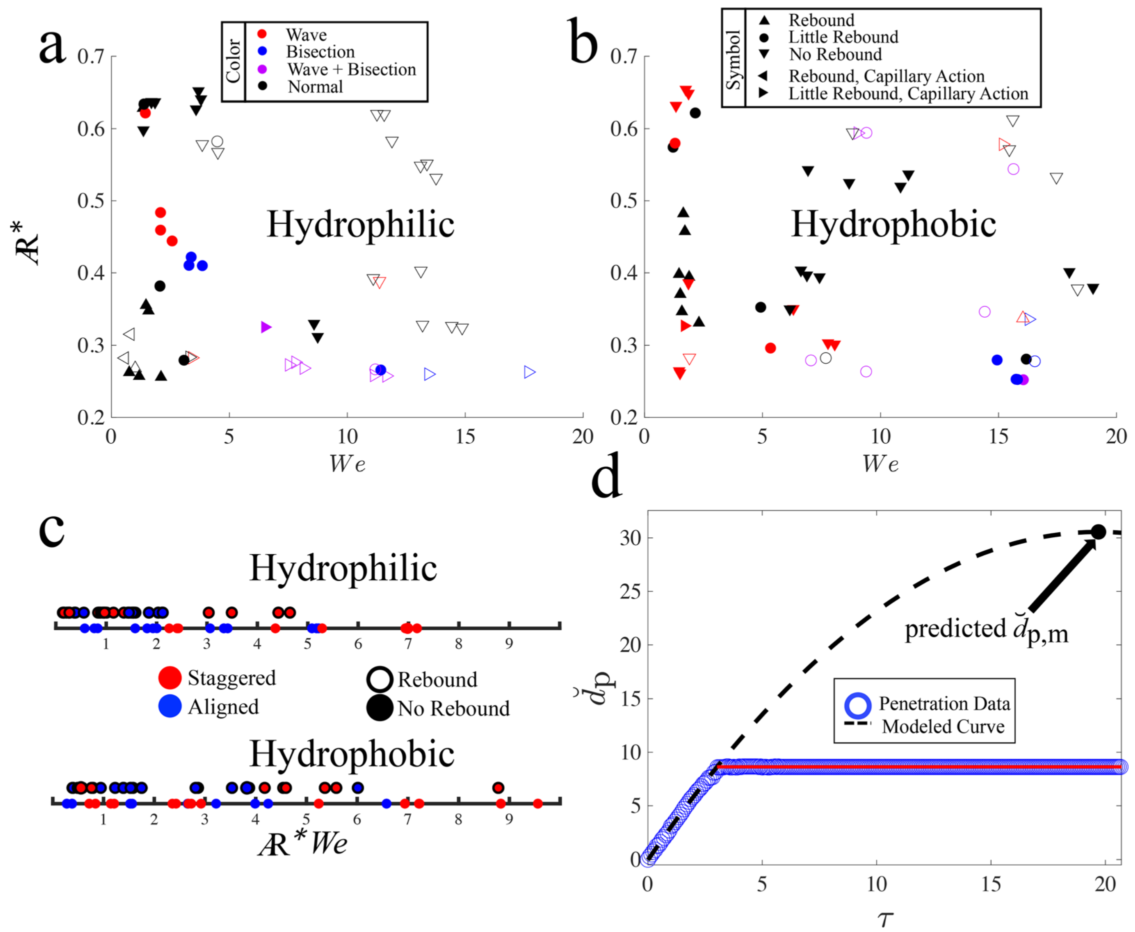

FIG. 5. (a,b) Modified aspect ratio AR$*$ vs We plot for observed impact classifications. Solid symbols (e.g., ■) represent impacts where the drop did not reach the bottom of the fiber array, whereas symbols with a black outline (e.g., □) represent impacts where the drop penetrated to the bottom of the fiber array. The legends above panels (a) and (b) apply to both. (c) Occurrence of drop rebound in the $AR * We$ spectrum in vertical fibers. (d) When the impacted drop reaches the base of the fiber array, a theoretical $\breve{d}_{p,m}$ can be predicted for when the fibers had "infinite" length by assuming a constant drop deceleration model. Multimedia available online.

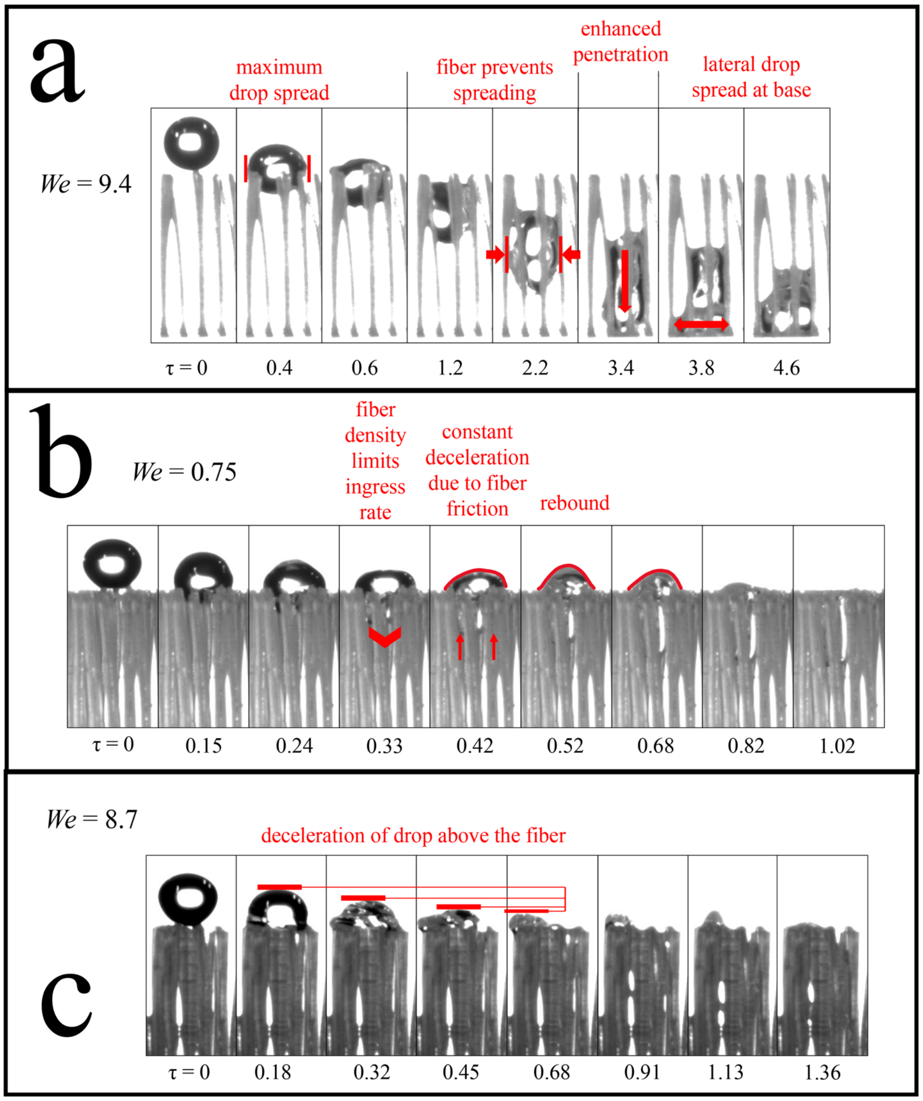

FIG. 6. Image sequences depicting various characteristics of drops impacting vertically oriented fiber arrays. (a) Drop maximum spread at the tip of the fibers at $\tau = 0.4$ before lateral drop spread ensues after the drop hits the bottom of the fiber array when $\tau > 3.4$. (b) Constant deceleration of liquid front within vertically oriented fiber arrays due to fiber friction and rebound above the fiber due to impact force. (c) Deceleration of drop above the fiber array due to impact force. Multimedia available online.

not investigate the temporal occurrences in drop evolution in this paper, we collectively classify each impact based on qualitative behaviors exhibited by the impacting liquid body until steady state is reached. By considering We and $\boldsymbol{AR}^*$, we find a superior predictor of impact behavior.[17] As in horizontally oriented fiber arrays,[17] the penetration of fiber arrays by impacting drops is, unsurprisingly, greatest for the least dense arrays and fastest drops.

B. Liquid penetration decelerates at a constant rate

We plot the penetration depth vs time of a drop impacting an array of density 50 strands/cm^2 at $We = 15.5$ in Fig. 5(d). In our experiments, we measure a constant deceleration of the penetrating liquid front due to drop interaction with the fiber shafts as shown in Figs. 6(b) and 5(d) (multimedia available online). Thus, when the drop reaches the base of the array, it is possible to predict the maximum penetration depth that would have been achieved by the drop body if the fibers had sufficient length. As fiber density increases, drops are more prone to rebound, as seen in Fig. 6(b), contributing to a greater impact force. When the rate of liquid ingress reaches a maximum at $\tau < 1$, the majority of the liquid mass resides above the array. Such mass rebounds as shown in Fig. 6(b), or its downward motion decelerates as shown in Fig. 6(c) (multimedia available online).

C. Penetration depth is characterized by an energy balance

Conservation of energy can be used to relate the maximum penetration depth $\breve{d}_{\rm p,m}$ to We. Since aligned and staggered fibers are equivalent to the impacting drop (Sec. II), we only consider aligned fibers in our model. A pre- and post-impact energy balance takes the form:

$$E_{\rm K} + E_{\rm S} = E'_{\rm S} + E'_{\rm D1} + E'_{\rm D2}, \tag{4}$$

where $E_K = \pi\rho D_0^3 U^2/12$ is the kinetic energy at impact and $E_S = \pi D_0^2 \sigma$ is the surface energy of a spherical drop. After impact, E'_S is the total final surface energy of the penetrated drop or fragments, E'_{D1} is the energy dissipated due to shear forces during impact, and E'_{D2} is the energy dissipated as the drop bulk spreads laterally on the tip of the fibers as discussed in our previous study.[17] The difference in potential energies before and after impact can be neglected in 1-cm tall arrays. Equation (4) applies rigid arrays of any density and for any impact type in which potential energy changes are negligible. In fibers that bend under the weight and capillary forces of a liquid body, the elastic energy can be quantified[47] and must be included in the energy balance. Although our fibers become slightly non-vertical after laser ablation, they do not bend under the force of the impacting drop as shown in Fig. 6(a) (multimedia available online) so that the elastic energy can be neglected.[31]

Viscous dissipation during impact can be derived using the same approach employed in a previous study on drop impacting hairy surfaces.[31] Upon impact, the spherical drop deforms into a cylinder intersected by fibers. For every fiber strand within the cylinder, the liquid body experiences shear on four sides of a square fiber. Each side of the fiber interacts with the liquid and is highlighted in pink in Fig. 7(a). The dissipation within the drop due to shear stress is[31] $E'_{D1} = \int_0^\tau \int_\Omega \Phi \mathrm{d}\Omega \, \mathrm{d}t \approx \Phi\Omega\tau$, where the viscous dissipation function is $\Phi \approx \mu U^2/a^2$, the volume of fluid over which dissipation takes place is $\Omega = \pi D_0^3/6$, and the timescale of dissipation upon impact is $\tau \approx d_{p,m}/U$ so that

$$E'_{D1} \approx \frac{\pi D_0^3}{6} \mu \frac{U d_{p,m}}{a^2}. \quad (5)$$

The vortical motions resulting in energy dissipation E'_{D2} occur as a result of an abrupt change of momentum when the impacting drop is forced to spread in the direction orthogonal to the impact velocity.[48] For a porous medium, E'_{D2} only occurs on the areas occupied by solid fibers at the topmost surface that first intercepts the drop shown as squares with red outline in Fig. 7(b). The areas occupied by the solid fibers in the circular projection of the drop is $\ell^2 D\pi\chi_s^2/4$. Therefore,[48]

$$E'_{D2} \approx \frac{1}{2}\ell^2 D E_K. \quad (6)$$

When $\ell^2 D \to 1$ in Eq. (6), the case of solid surface is recovered.

The front view projection of the liquid body that penetrated within the fiber array is rectangular, as illustrated in Fig. 7(c). The impacting drop initially has a circular top view projection when it impacts the fibers as shown by the blue solid circle in Fig. 7(b), and so the penetration depth along the centerline of the drop is necessarily greater than at the edges. Simultaneously, the top-down profile of the drop at steady-state conforms to the fiber array structure so that it resembles a rectangular prism, outlined by the dashed rectangle in Fig. 7(b). We, thus, approximate the final shape of the drop as a rectangular prism. For a hexagonal array structure, the steady-state shape of the drop will be cylindrical.[31] An image sequence experimentally showing such a transition is shown in Fig. 7(d). The number of strands within the rectangular prism comprised by the liquid body is $D\chi_s^2$. Each square strand has an area $4\ell d_{p,m}$ that is interacting with water as shown in Fig. 7(a). The total surface energy due to the interaction of the liquid body with the fiber strands is $4\ell d_{p,m} D\chi_s^2 \sigma(-\cos\theta_e)$. On the sides of the liquid, the area interacting with air is $\boldsymbol{AR}\chi_s d_{p,m}$ colored blue in Fig. 7(c). On the top or bottom surface of the liquid, the area interacting with air is $(1 - D\ell^2)\chi_s^2$ [fiber strands within the blue dashed square in Fig. 7(b)]. Thus, the total surface energy after impact is

$$E'_S = 4\ell d_{p,m} D\chi_s^2 \sigma(-\cos\theta_e) + 4\boldsymbol{AR}\chi_s d_{p,m}\sigma + 2(1 - D\ell^2)\chi_s^2\sigma. \quad (7)$$

The value of $E'_{D1} + E'_{D2} \ll E'_S$ is by two or more orders of magnitude for the range of U we test so that E'_{D1} and E'_{D2} can be neglected in an energy balance. When the fibers are vertical, spreading is restricted

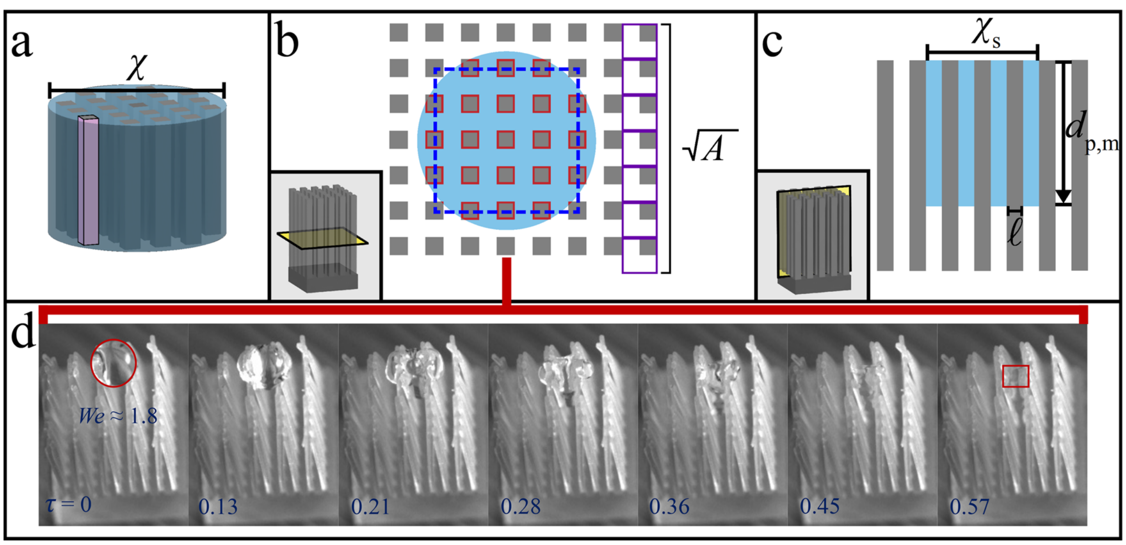

FIG. 7. Graphical accompaniment to the penetration depth model. The view of fibers shown in each panel is indicated by the lightly colored planes in each inset where an inset appears. (a) Cylindrical model of impacting drop before achieving steady state. (b) Top view of cylindrical impacting drop. (c) Side view of impacted drop. (d) Image sequence showing the transition of the area projection of the drop from circular to rectangular.

so that $\chi_s \approx \epsilon D_0$ as demonstrated in Fig. 6(a). The energy balance in Eq. (4) can be written as

$$\frac{\pi}{48\left[\epsilon^2 \ell D D_0(-\cos\theta_e) + \epsilon \dfrac{a}{\ell + a}\right]} \frac{\rho D_0 U^2}{\sigma} + \frac{\pi - 2\epsilon^2 + 2\epsilon^2 D\ell^2}{4\left[\epsilon^2 \ell D D_0(-\cos\theta_e) + \epsilon \dfrac{a}{\ell + a}\right]} \approx \frac{d_{p,m}}{D_0}. \quad (8)$$

In our fiber arrays, $\epsilon \approx 0.7$. Fiber density may be expressed as a function of a and ℓ. For a square aligned fiber array of area A, one side of the square is of length $\sqrt{A}$ as illustrated in Fig. 7(b). The fiber array can be subdivided into repeating square units of length $(\ell + a)$ shown as purple boxes in Fig. 7(b) so that the total number of rows in a fiber array is $\sqrt{A}/(\ell + a)$. Each repeating unit contains a single fiber strand as shown in Fig. 7(b). Thus, the total number of strands in A is $A/(\ell + a)^2$ so that $D = 1/(\ell + a)^2$. Rewriting Eq. (8) in terms of We and nondimensionalizing by Eq. (3)

$$\breve{d}_{p,s} \approx k_1 We + k_2. \quad (9)$$

The dynamic coefficient

$$k_1 = \frac{\pi(\ell + a)}{48\left[\epsilon^2 D_0 \dfrac{\ell}{\ell + a}(-\cos\theta_e) + \epsilon a\right]}, \quad (10)$$

and the static coefficient

$$k_2 = \frac{(\pi - 2\epsilon^2)(\ell + a) + 2\epsilon^2 \dfrac{\ell^2}{\ell + a}}{4\left[\epsilon^2 D_0 \dfrac{\ell}{\ell + a}(-\cos\theta_e) + \epsilon a\right]}. \quad (11)$$

The behavior of k_1 and k_2 is dependent on strand wettability and the range of a or equivalently, D. For hydrophilic fibers, it is possible to choose a contact angle for which the denominators of Eqs. (10) and (11) become zero, a vulnerability with denser fibers. The asymptotic quirk of our model can be mitigated, if needed for denser fibers, by imposing conservation of volume, $\pi D_0^3/6 = \chi_s^2 d_{p,m} - \{1 - [\ell^2/(\ell + a)^2]\}\chi_s^2 \ell^2 d_{p,m}$, on Eq. (7). Doing so makes a prediction of penetration depth [Eq. (9)] that is slightly nonlinear and implicit.

Because of length limitation of our fiber arrays, we employ the constant deceleration model discussed in Sec. III B to predict the maximum penetration depth $d_{p,m}$ for impacts where the liquid body reached the bottom of the fiber array. The predicted $d_{p,m}$, an extrapolation, is highly sensitive to the temporal position of the drop leading to the collision of the drop with the base of the fiber array, resulting in large standard deviations in our predicted data.

Penetration depth values are measured before capillary creep that occurs on the timescale of multiple seconds. A plot of $\breve{d}_{p,m}$ vs We following Eq. (9) and the corresponding test for linearity Pearson correlation coefficient r values are shown in Fig. 8. Penetration depth increases linearly with We when the fibers are sparse. At higher fiber

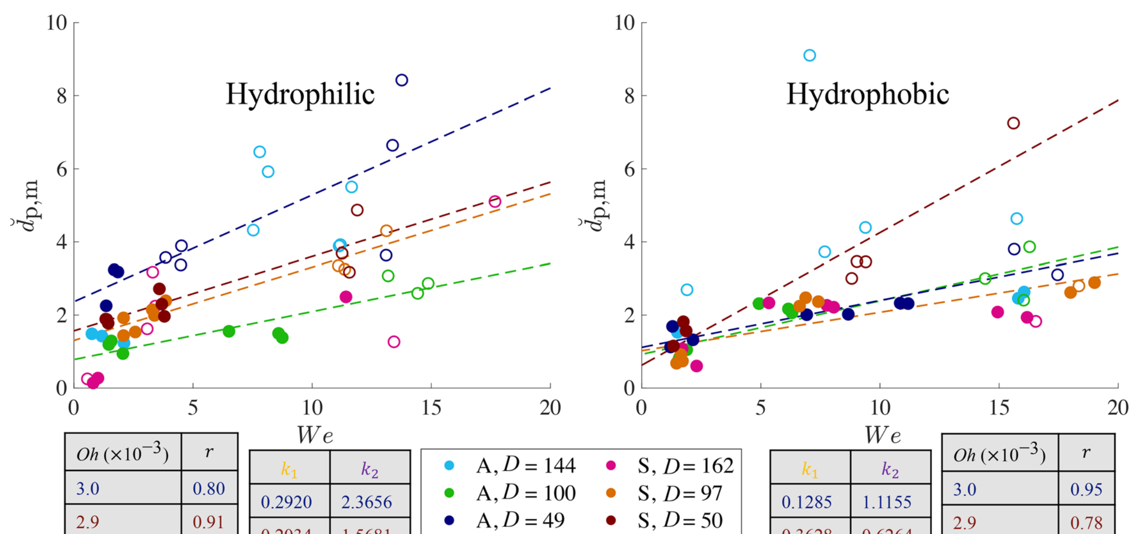

Hydrophilic:

Oh ($\times 10^{-3}$)	r
3.0	0.80
2.9	0.91
3.9	0.88
3.6	0.91
4.5	0.77
4.3	0.67

k_1	k_2
0.2920	2.3656
0.2034	1.5681
0.1314	0.7807
0.2005	1.3047

Hydrophobic:

k_1	k_2
0.1285	1.1155
0.3628	0.6264
0.1467	0.9229
0.1053	1.0233

Oh ($\times 10^{-3}$)	r
3.0	0.95
2.9	0.78
3.9	0.88
3.6	0.84
4.5	0.18
4.3	0.63

FIG. 8. Normalized maximum penetration depth vs Weber number. Solid symbols (●) use the experimentally measured penetration depth for cases wherein the penetrated liquid did not reach the bottom of the fiber array, whereas hollow symbols (○) use the penetration depth value predicted by the constant deceleration model for cases, wherein the penetrated liquid reached the bottom of the fiber array. Linear coefficients k_1 and k_2 according to Eq. (9) are provided in fiber densities where the Pearson correlation coefficient is $r > 0.8$. Fibers are either aligned (A) or staggered (S) and have a packing density D.

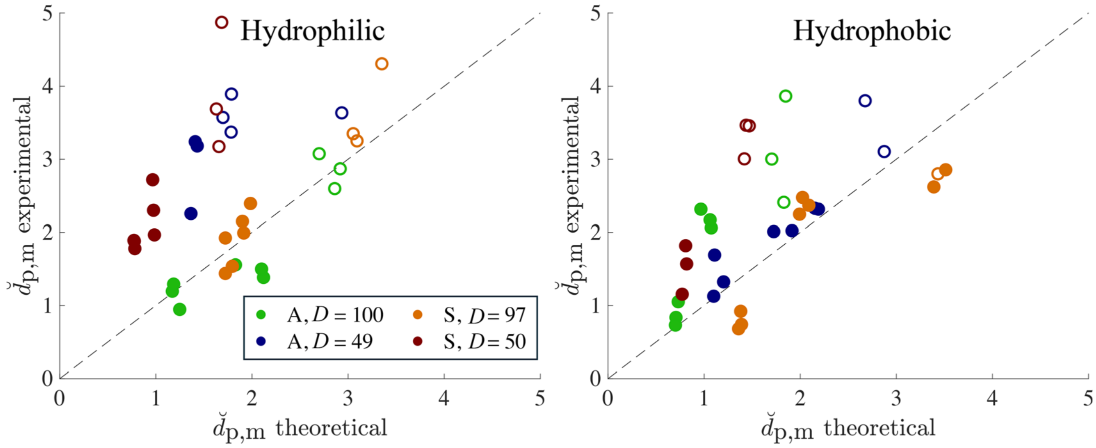

FIG. 9. Plots of experimental normalized maximum penetration depth vs the theoretical values predicted in Eqs. (10) and (11). Black line represents $\breve{d}_{\mathrm{p,m}}$ experimental $= \breve{d}_{\mathrm{p,m}}$ theoretical. Solid symbols (●) use the experimentally measured penetration depth for cases wherein the penetrated liquid did not reach the bottom of the fiber array, whereas hollow symbols (○) use the penetration depth value predicted by the constant deceleration model as the $\breve{d}_{\mathrm{p,m}}$ experimental for cases wherein the penetrated liquid reached the bottom of the fiber array. Fibers are either aligned (A) or staggered (S) and have a packing density D. Experimental data in which $Oh > 4 \times 10^{-3}$ are omitted when comparing predicted experimental vs theoretical values of $\breve{d}_{\mathrm{p,m}}$.

densities, a lower a makes the viscous dissipation E'_{D1} significant such that it must be included in an energy balance. Thus, our model predicts a nonlinear relationship between penetration depth and We at higher fiber densities. When fiber density produces $Oh \gtrsim 4 \times 10^{-3}$, we experimentally confirm that $\breve{d}_{\mathrm{p,m}}$ non-linearly decreases with We with a Pearson correlation coefficient $r < 78\%$. As expected, experimental hydrophilic fibers have a higher static coefficient k_2 than their hydrophobic counterparts due to enhanced capillary effects. We plot experimental vs model values of $\breve{d}_{\mathrm{p,m}}$ in Fig. 9. Generally, our model under-predicts penetration depth, particularly for sparse, hydrophilic fibers. For these conditions, drops penetrate to the fiber base, and so the experimental value we report may be an overestimation. The remaining under-predictions of our model are likely a result of the assumption that the drop remains tied to the fiber tips when calculating the post-impact surface energy in Eq. (5). However, if the drop falls past the fiber tips, the reported $\breve{d}_{\mathrm{p,m}}$ is necessarily greater than the model value. Our model of surface energy is also limited when $\ell^2 D \to 1$ and [intuitively] $d_{\mathrm{p,m}} \to 0$ in the case of a solid surface.

Our results suggest that hydrophilic vertical fibers are functionally poor for water repellency, even though hydrophilic horizontal fibers form a dynamic drop barrier under certain conditions, as shown in our previous work.[17] The rebound of drops, which we show to be promoted by fiber packing density, is a mechanism to repel water. In colder environments where staying dry is needed for thermoregulation, animals carry denser fur than animals in hotter environments where wetting of the skin and the resultant evaporation is a means of cooling.[49,50] We investigate drop impacts with $U < 0.7$ m/s, $We < 20$ and show that the penetration depth increases linearly with We whenever $Oh \lesssim 4 \times 10^{-3}$. Since vertical fibers prevent drop fragmentation, we expect our results to extend to impact speeds of raindrops. The penetration depth of impacting drops is greater in vertically oriented fibers than in horizontally oriented counterparts. Our work provides possible physical causality for why fur lays flat on the animal body, oriented horizontally with respect to falling rain, except during discrete social events.[51–54]

IV. CONCLUSIONS

Drops decelerate at a constant rate within vertical fiber arrays. Conservation of energy provides a linear relation between drop penetration depth into vertical fibers and the Weber number, a relationship that is experimentally validated for sparse fibers of various packing density, fiber alignments, and wettability. When fiber density produces $Oh \gtrsim 4 \times 10^{-3}$, penetration depth decreases for $We \gtrsim 10$. Anisotropic misalignment in vertical fibers induces lateral drop motions, which are promoted by a low We, and high fiber packing density or equivalently a low $\boldsymbol{AR}^*$. Like with horizontal fibers, a lower $\boldsymbol{AR}^* We$ promotes drop rebound upon impact. In hydrophobic fibers, the penetration depth decreases with increasing fiber packing density, as expected. Capillary action in vertical fibers promotes penetration and prevents spreading. A penetration model based on kinetic and surface energies well-predicts the magnitude of penetration into vertical fibers, a prediction that is linear with Weber number for sparse fibers. Future works could consider longer and denser arrays as well as higher drop impact speeds.

ACKNOWLEDGMENTS

This research was partially funded by the National Science Foundation (CMMI 1825801 and CBET 2205558). We thank undergraduate research assistants at the Fluids and Structures Laboratory, Syed Jaffar Raza for bespoke code contributions, Alexander Bottoms for editing some of the supplementary videos, and Michael Spinazzola III for fine-tuning the laser-cutting setup and parameters for our vertical fiber arrays. We also give special thanks to Mohammad Alipanahrostami for coating our samples.

AUTHOR DECLARATIONS

Conflict of Interest

The authors have no conflicts to disclose.

Author Contributions

Gene Patrick S. Rible: Conceptualization (equal); Data curation (lead); Formal analysis (lead); Investigation (lead); Methodology (lead); Visualization (lead); Writing – original draft (equal); Writing – review & editing (equal). **Visalsaya Chakpuang:** Data curation (supporting); Investigation (supporting). **Aidan D. Holihan:** Data curation (supporting); Investigation (supporting). **Hannah P. Sebek:** Data curation (supporting); Investigation (supporting). **Hannah H. Osman:** Data curation (supporting); Investigation (supporting). **Kyle R. Brown:** Data curation (supporting); Investigation (supporting). **Wei Wang:** Resources (equal). **Andrew K. Dickerson:** Conceptualization (equal); Funding acquisition (lead); Project administration (lead); Writing – original draft (equal); Writing – review & editing (equal).

DATA AVAILABILITY

The data that support the findings of this study are available from the corresponding author upon reasonable request.

REFERENCES

[1]T. J. Dawson, K. N. Webster, and S. K. Maloney, "The fur of mammals in exposed environments; do crypsis and thermal needs necessarily conflict? the polar bear and marsupial koala compared," J. Comp. Physiol. B **184**, 273–284 (2014).
[2]W. Montagna, "Comparative anatomy and physiology of the skin," Arch. Dermatol. **96**, 357–363 (1967).
[3]D. Mota-Rojas, C. G. Titto, A. de Mira Geraldo, J. Martínez-Burnes, J. Gómez, I. Hernández-Ávalos, A. Casas, A. Domínguez, N. José, A. Bertoni *et al.*, "Efficacy and function of feathers, hair, and glabrous skin in the thermoregulation strategies of domestic animals," Animals **11**, 3472 (2021).
[4]H. E. Liwanag, A. Berta, D. P. Costa, M. Abney, and T. M. Williams, "Morphological and thermal properties of mammalian insulation: The evolution of fur for aquatic living," Biol. J. Linn. Soc. **106**, 926–939 (2012).
[5]I. M. Baker, "Infrared antenna-like structures in mammalian fur," Roy. Soc. Open Sci. **8**, 210740 (2021).
[6]A. K. Dickerson, Z. G. Mills, and D. L. Hu, "Wet mammals shake at tuned frequencies to dry," J R Soc. Interface **9**, 3208–3218 (2012).
[7]T. D. Williams, D. D. Allen, J. M. Groff, and R. L. Glass, "An analysis of California sea otter (enhydra lutris) pelage and integument," Mar. Mammal Sci. **8**, 1–18 (1992).
[8]R. Tregear, "Hair density, wind speed, and heat loss in mammals," J. Appl. Physiol. **20**, 796–801 (1965).
[9]E. R. Oyer, "Identification of mammals from studies of hair structure," Trans. Kansas Acad. Sci. **49**, 155–160 (1946).
[10]P. Soppela, M. Nieminen, and J. Timisjärvi, "Thermoregulation in reindeer," Rangifer **6**, 273–278 (1986).
[11]A. Domínguez-Oliva, M. D. Ghezzi, P. Mora-Medina, I. Hernández-Ávalos, J. Jacome, A. Castellón, I. Falcón, F. Reséndiz, N. Romero, R. Ponce *et al.*, "Anatomical, physiological, and behavioral mechanisms of thermoregulation in elephants," J. Anim. Behav. Biometeorol. **10**, 1–0 (2022).
[12]J. W. Weisel, C. Nagaswami, and R. O. Peterson, "River otter hair structure facilitates interlocking to impede penetration of water and allow trapping of air," Can. J. Zool. **83**, 649–655 (2005).
[13]W. Landauer, "On the hair direction in mammals," J. Mammal. **6**, 217–232 (1925).
[14]M. Krsmanovic, H. Ali, D. Biswas, R. Ghosh, and A. K. Dickerson, "Fouling of mammalian hair fibres exposed to a titanium dioxide colloidal suspension," J. R. Soc. Interface **19**, 20210904 (2022).
[15]M. Krsmanovic, R. Ghosh, and A. K. Dickerson, "Fur flutter in fluid flow fends off foulers," J. R Soc. Interface **20**, 20230485 (2023).
[16]A. P. Lebanoff and A. K. Dickerson, "Drop impact onto pine needle fibers with non-circular cross section," Phys. Fluids **32**, 092113 (2020).
[17]G. P. S. Rible, M. A. Spinazzola, III, R. E. Jones, III, R. U. Constantin, W. Wang, and A. K. Dickerson, "Dynamic drop penetration of horizontally oriented fiber arrays," Langmuir **40**, 13339 (2024).
[18]M. Safavi and S. Nourazar, "Experimental, analytical, and numerical study of droplet impact on a horizontal fiber," Int. J. Multiphase Flow **113**, 316–324 (2019).
[19]S.-G. Kim and W. Kim, "Drop impact on a fiber," Phys. Fluids **28**, 042001 (2016).
[20]Y.-Y. Tang, M.-J. Su, G.-W. Chu, Y. Luo, Y.-Y. Wang, L.-L. Zhang, and J.-F. Chen, "Impact phenomena of liquid droplet passing through stainless steel wire mesh units," Chem. Eng. Sci. **198**, 144–154 (2019).
[21]N. Ojaghlou, H. V. Tafreshi, D. Bratko, and A. Luzar, "Dynamical insights into the mechanism of a droplet detachment from a fiber," Soft Matter **14**, 8924–8934 (2018).
[22]W. Gu, S. Yan, and Z. Bai, "A study on a droplet impact on a fiber during coalescence-separation: Phenomena and models," Chem. Eng. Sci. **212**, 115337 (2020).
[23]G. Zhang, M. A. Quetzeri-Santiago, C. A. Stone, L. Botto, and J. R. Castrejón-Pita, "Droplet impact dynamics on textiles," Soft Matter **14**, 8182–8190 (2018).
[24]D. J. Bouchard, "Droplet impact, infiltration, and boiling in pores and porous media," PhD thesis (University of Toronto, 2021).
[25]I. V. Roisman, A. Lembach, and C. Tropea, "Drop splashing induced by target roughness and porosity: The size plays no role," Adv. Colloid Interface Sci. **222**, 615–621 (2015).
[26]É. Lorenceau and D. Quéré, "Drops impacting a sieve," J. Colloid Interface Sci. **263**, 244–249 (2003).
[27]K. Cardin, C. Josserand, and R. B. Cal, "Droplet capture in a fiber array," Phys. Rev. Fluids **8**, 043601 (2023).
[28]A. Delbos, E. Lorenceau, and O. Pitois, "Forced impregnation of a capillary tube with drop impact," J. Colloid Interface Sci. **341**, 171–177 (2010).
[29]A. Kumar and S. Hartland, "Shape of a drop on a vertical fiber," J. Colloid Interface Sci. **124**, 67–76 (1988).
[30]M. Radiom, W. K. Chan, and C. Yang, "A study of capillary flow from a pendant droplet," Microfluid. Nanofluid. **7**, 697–707 (2009).
[31]A. Nasto, P.-T. Brun, and A. E. Hosoi, "Drop impact on hairy surfaces," Phys. Rev. Fluids **4**, 064004 (2019).
[32]C. Tang, M. Qin, X. Weng, X. Zhang, P. Zhang, J. Li, and Z. Huang, "Dynamics of droplet impact on solid surface with different roughness," Int. J. Multiphase Flow **96**, 56–69 (2017).
[33]A. N. Lembach, H.-B. Tan, I. V. Roisman, T. Gambaryan-Roisman, Y. Zhang, C. Tropea, and A. L. Yarin, "Drop impact, spreading, splashing, and penetration into electrospun nanofiber mats," Langmuir **26**, 9516–9523 (2010).
[34]D. Bouchard and S. Chandra, "Infiltration of impacting droplets into porous substrates," Experiments Fluids **61**, 1–16 (2020).
[35]R. K. Holman, M. J. Cima, S. A. Uhland, and E. Sachs, "Spreading and infiltration of inkjet-printed polymer solution droplets on a porous substrate," J. Colloid Interface Sci. **249**, 432–440 (2002).
[36]P. Zhu, W. Wang, X. Chen, F. Lin, X. Wei, C. Ji, and J. Zou, "Experimental study of drop impact on a thin fiber," Phys. Fluids **31**, 107102 (2019).
[37]R. Labbé and C. Duprat, "Capturing aerosol droplets with fibers," Soft Matter **15**, 6946–6951 (2019).
[38]C. Duprat, S. Protiere, A. Beebe, and H. A. Stone, "Wetting of flexible fibre arrays," Nature **482**, 510–513 (2012).
[39]M. W. Kulbaba, "Investigating epizoochorous adaptations to mammalian furs," PhD thesis, (Department of Biology, University of Winnipeg, 2004).
[40]R. Mihaylov and K. Kirilov, "Morphological study on hairs from mammalian predators in Bulgaria," 2022.
[41]A. Tokay, W. A. Petersen, P. Gatlin, and M. Wingo, "Comparison of raindrop size distribution measurements by collocated disdrometers," J. Atmos. Ocean. Technol. **30**, 1672–1690 (2013).
[42]W. Wang, X. Du, H. Vahabi, S. Zhao, Y. Yin, A. K. Kota, and T. Tong, "Trade-off in membrane distillation with monolithic omniphobic membranes," Nat. Commun. **10**, 3220 (2019).
[43]W. Wang, J. Salazar, H. Vahabi, A. Joshi-Imre, W. E. Voit, and A. K. Kota, "Metamorphic superomniphobic surfaces," Adv. Mater. **29**, 1700295 (2017).
[44]M. Cichomski, K. Kośla, W. Pawlak, W. Kozłowski, and W. Szmaja, "Stability and tribological investigations of 1h, 1h, 2h, 2h-perfluoroalkyltrichlorosilane on titania surface," Tribol. Int. **77**, 1–6 (2014).

[45]M. Cichomski, K. Kośla, W. Kozłowski, W. Szmaja, J. Balcerski, J. Rogowski, and J. Grobelny, "Investigation of the structure of fluoroalkylsilanes deposited on alumina surface," Appl. Surf. Sci. **258**, 9849–9855 (2012).
[46]P. J. Pritchard and J. W. Mitchell, *Fox and McDonald's Introduction to Fluid Mechanics* (John Wiley & Sons, 2016).
[47]J. Bico, B. Roman, L. Moulin, and A. Boudaoud, "Elastocapillary coalescence in wet hair," Nature **432**, 690–690 (2004).
[48]S. Wildeman, C. W. Visser, C. Sun, and D. Lohse, "On the spreading of impacting drops," J. Fluid Mech. **805**, 636–655 (2016).
[49]S. A. Oswald, S. Bearhop, R. W. Furness, B. Huntley, and K. C. Hamer, "Heat stress in a high-latitude seabird: Effects of temperature and food supply on bathing and nest attendance of great skuas Catharacta skua," J. Avian Biol. **39**, 163–169 (2008).
[50]E. T. Krause and T. Ruploh, "Captive domesticated zebra finches (Taeniopygia guttata) have increased plasma corticosterone concentrations in the absence of bathing water," Appl. Anim. Behav. Sci. **182**, 80–85 (2016).
[51]G. Chaplin, N. G. Jablonski, R. W. Sussman, and E. A. Kelley, "The role of piloerection in primate thermoregulation," Folia Primatol. **85**, 1–17 (2013).
[52]J. D. Pruetz, T. C. LaDuke, and K. Dobson, 2022 "Savanna chimpanzees (pan troglodytes verus) in senegal react to deadly snakes and other reptiles: Testing the snake detection hypothesis," bioRxiv, pp. 2022–09.
[53]R. Heesen, D. A. Austry, Z. Upton, and Z. Clay, "Flexible signalling strategies by victims mediate post-conflict interactions in bonobos," Philos. Trans. R. Soc. **B377**, 20210310 (2022).
[54]M. N. Muller and R. W. Wrangham, "Dominance, aggression and testosterone in wild chimpanzees: A test of the 'challenge hypothesis,'" Anim. Behav. **67**, 113–123 (2004).